

Rhombic Grids Reduce the Number of Voxels in Fast Pulse-Echo Ultrasound Imaging

Martin F. Schiffner


Chair of Medical Engineering, Ruhr-University Bochum, 44801 Bochum, Germany

Copyright notice:

© 2022 IEEE. Personal use of this material is permitted. Permission from IEEE must be obtained for all other uses, in any current or future media, including reprinting/republishing this material for advertising or promotional purposes, creating new collective works, for resale or redistribution to servers or lists, or reuse of any copyrighted component of this work in other works.

To be published in the proceedings of the IEEE International Ultrasonics Symposium (IUS), Venice, Italy, Oct. 2022.

Rhombic Grids Reduce the Number of Voxels in Fast Pulse-Echo Ultrasound Imaging

Martin F. Schiffner 
 Chair of Medical Engineering
 Ruhr-University Bochum
 Bochum, Germany
 martin.schiffner@rub.de

Abstract—Ultrafast imaging modes, such as coherent plane-wave compounding (CPWC), capture a large field of view in a single pulse-echo measurement using parallel receive focusing. The number of foci or, equivalently, the number of volume elements (voxels) in the image determines the computational costs and the memory consumption of the image formation. Herein, 120° rhombic grids are proposed to specify the voxel positions and reduce the number of voxels in comparison to orthogonal grids. The proposed grids derive from the bivariate sampling theorem and the spectral properties of the images formed by the delay-and-sum algorithm in CPWC. A phantom experiment validated the proposed grids and showed reductions in the number of voxels by 81.4% and 14.7% in comparison to the usual and optimal orthogonal grids, respectively. Mean structural similarity indices above 96.6% and relative root mean-squared errors below 6.8% confirmed the visual equivalence of all images after interpolations to the usual orthogonal grid.

Index Terms—rhombic grids, optimal orthogonal grids, bivariate sampling theorem, fast ultrasound imaging, voxel-based beamforming, point scatterers, spectral properties

I. INTRODUCTION

Ultrafast imaging modes, such as coherent plane-wave compounding (CPWC) [1], use software to form complete images from single pulse-echo measurements [2]. Image formation algorithms, such as delay-and-sum (DAS) [3] or constrained ℓ_q -minimization [4], [5], discretize the object to be imaged using point scatterers on an orthogonal grid. Each point scatterer represents a volume element (voxel) of the object. The grid of point scatterers exactly represents the entire object if the grid spacings are sufficiently small. The limited bandwidth of the pulse-echo measurements, then, makes the grid of point scatterers indistinguishable from the object. The algorithms, however, must compute the strengths of all point scatterers. The DAS algorithm, for example, measures the amplitude of the echo received from each scatterer by parallel focusing. Since the number of point scatterers determines the computational costs and the memory consumption, it is important to find grids that not only enable an exact object representation but also minimize the number of voxels.

Herein, rhombic grids are proposed to reduce the number of voxels and, thus, the computational costs and the memory consumption of the image formation. The spectral properties of the images formed by the DAS algorithm in CPWC will be reviewed first. These properties will subsequently be inserted into the bivariate sampling theorem [6] to derive two grids

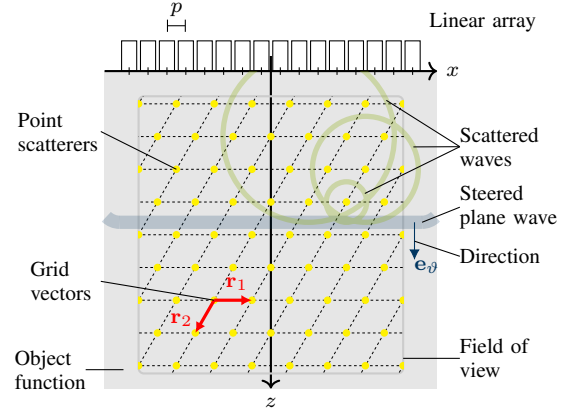


Fig. 1. Discretization of the object function using point scatterers on a regular grid. The object function describes spatial fluctuations in the acoustic object properties. The pulse-echo measurements, owing to the limited bandwidth, cannot distinguish the grid of point scatterers from the object.

that enable an exact object representation. The first grid is an optimal orthogonal grid. The second grid is the proposed rhombic grid. A phantom experiment will eventually show the advantages of the rhombic grid over the usual and optimal orthogonal grids.

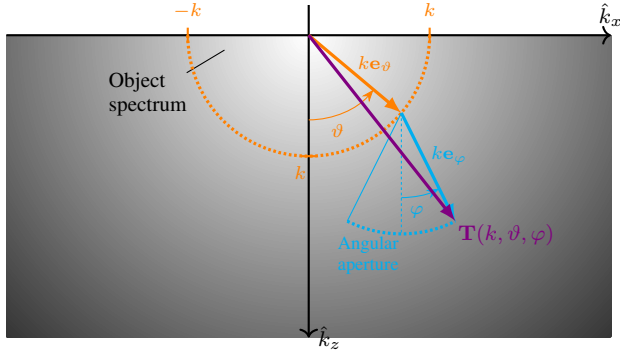
II. THEORY

This paper exclusively treats pulse-echo measurements with steered plane waves (PWs), as shown in Fig. 1. A linear array with the pitch p serves as transducer. All grid types are regular (i.e., the shapes of all voxels are equal).

A. Spectral Properties of Ultrasound Images

Ultrasound images are bandpass-filtered versions of the acoustic object function. This function describes the spatial fluctuations in the acoustic properties of the object to be imaged. The bounded passbands, as will be shown in Sect. II-B, enable grids of point scatterers to emulate the object function in the image formation. The optimal grid parameters, however, depend on the exact shapes of the passbands. This section, hence, will review the passbands of the images formed by the DAS algorithm in CPWC. The maximum passbands, according to the Fourier diffraction theorem [7, Theorem 8.4], [8], exclusively depend on the steering angles and the

(a) Monofrequent steered plane wave



(b) Sequence of three steered plane waves

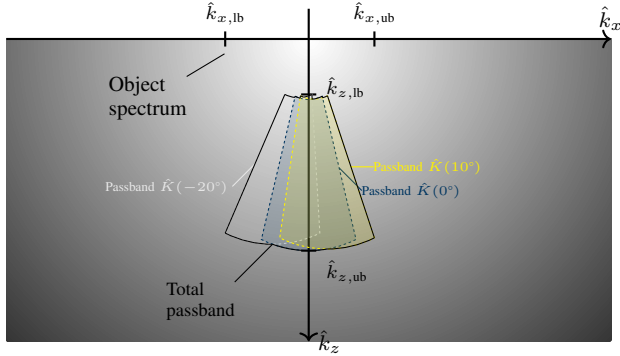


Fig. 2. The DAS algorithm bandpass filters the object function. The algorithm, fixing both the wavenumber $k > 0$ and the steering angle $\vartheta \in (-\pi/2; \pi/2)$, recovers the object spectrum on (a) the circular arc with the center $k\mathbf{e}_\vartheta$ and the radius k . The angular aperture, which derives from the F -number, limits the receive angle φ . A sequence of $N = 3$ plane-wave measurements, varying the wavenumber k within the interval $k \in [k_{lb}; k_{ub}]$, where $k_{lb} > 0$ and $k_{ub} > k_{lb}$ denote the lower and upper endpoints, respectively, recovers the object spectrum in (b) the union (2) with the extremal angular spatial frequencies (3).

bandwidth of the acquired radio frequency (RF) signals. The array geometry, the measurement noise, and additional signal processing methods, such as grating and side lobe suppression, however, can reduce the recoverable passbands.

1) *Single Plane-Wave Images*: A single plane-wave measurement enables the formation of a low-quality image. The recoverable passband $\hat{K}(\vartheta)$ for a PW with the steering angle $\vartheta \in (-\pi/2; \pi/2)$ equals

$$\hat{K}(\vartheta) = \left\{ \hat{\mathbf{k}} \in \mathbb{R}^2 : \hat{\mathbf{k}} = \mathbf{T}(k, \vartheta, \varphi), \right. \\ \left. (k, \varphi) \in [k_{lb}; k_{ub}] \times [\varphi_{lb}; \varphi_{ub}] \right\}, \quad (1a)$$

where \mathbf{T} is the coordinate transform

$$\mathbf{T}(k, \vartheta, \varphi) = k(\mathbf{e}_\vartheta + \mathbf{e}_\varphi) \quad (1b)$$

with the wavenumber $k > 0$, the receive angle $\varphi \in (-\pi/2; \pi/2)$, and the unit vectors $\mathbf{e}_\vartheta = (\sin(\vartheta), \cos(\vartheta))^T$ and $\mathbf{e}_\varphi = (\sin(\varphi), \cos(\varphi))^T$. This transform, for a given steering angle ϑ , maps the wavenumber k and the receive angle φ to the angular spatial frequencies $\hat{\mathbf{k}} = (\hat{k}_x, \hat{k}_z)^T$. These frequencies, fixing the wavenumber k , form a circular arc with the center

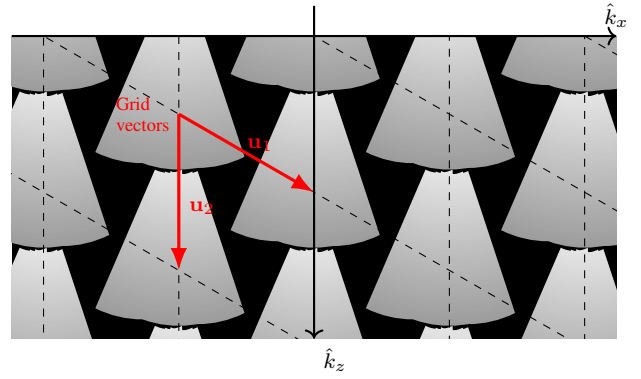


Fig. 3. Effect of the discretization of the bandpass-filtered object function. The discretization superimposes copies of the object spectrum in the spatial Fourier domain. These copies are limited to the total recoverable passband (2) and arise on the regular grid (5). The bandpass-filtered object function and, thus, the ultrasound image can be recovered from this superposition if the grid vectors \mathbf{u}_1 and \mathbf{u}_2 prevent the copies from overlapping. Given suitable spectral grid vectors \mathbf{u}_1 and \mathbf{u}_2 , the spatial grid vectors \mathbf{r}_1 and \mathbf{r}_2 equal (6).

$k\mathbf{e}_\vartheta$ and the radius k , as shown in Fig. 2(a). The angular aperture of this arc derives from the F -number $F > 0$ in the receive focusing [9] and imposes the lower and upper bounds $\varphi_{lb} = -\varphi_{ub}$ and $\varphi_{ub} = \arctan(1/(2F))$, respectively, on the receive angle φ . The wavenumber k has the lower and upper bounds $k_{lb} > 0$ and $k_{ub} > k_{lb}$, respectively, because of the limited bandwidth of the acquired RF signals.

2) *Plane-Wave Compound Images*: The superposition of the low-quality images obtained from a sequence of $N \in \mathbb{N}$ plane-wave measurements improves the image quality at the expense of the frame rate. The recoverable passbands (1) for the steering angles $\vartheta_0 < \vartheta_1 < \dots < \vartheta_{N-1}$, as shown in Fig. 2(b), merge into the total recoverable passband

$$\hat{K} = \bigcup_{n=0}^{N-1} \hat{K}(\vartheta_n). \quad (2)$$

This enlarged passband explains the higher image quality and defines the bounds on the angular spatial frequencies

$$\hat{k}_{x,lb} = k_{ub}[\sin(\vartheta_0) - \sin(\varphi_{ub})], \quad (3a)$$

$$\hat{k}_{x,ub} = k_{ub}[\sin(\vartheta_{N-1}) + \sin(\varphi_{ub})], \quad (3b)$$

$$\hat{k}_{z,lb} = k_{lb}[\min\{\cos(\vartheta_0), \cos(\vartheta_{N-1})\} + \cos(\varphi_{ub})], \quad (3c)$$

$$\hat{k}_{z,ub} = k_{ub}[\max_n\{\cos(\vartheta_n)\} + 1], \quad (3d)$$

which will now be used in the optimization of the grid parameters.

B. Sampling of Ultrasound Images

The image, as explained in Sect. II-A, at best equals the bandpass-filtered object function. The spectrum of this function equals the spectrum of the object function inside the total recoverable passband (2) but zero elsewhere. Such a function, according to the bivariate sampling theorem [6], can be recovered from its samples on the regular grid

$$\mathbb{G} = \{\mathbf{r} \in \mathbb{R}^2 : \mathbf{r} = l_1\mathbf{r}_1 + l_2\mathbf{r}_2, l_1, l_2 \in \mathbb{Z}\}, \quad (4)$$

where \mathbb{Z} is the set of all integers and \mathbf{r}_1 and \mathbf{r}_2 are linearly independent vectors that will now be determined.

The sampling superimposes copies of the bandpass-filtered object spectrum in the spatial Fourier domain, as shown in Fig. 3. These copies arise at all points of the regular grid

$$\mathbb{H} = \{\mathbf{u} \in \mathbb{R}^2 : \mathbf{u} = m_1 \mathbf{u}_1 + m_2 \mathbf{u}_2, m_1, m_2 \in \mathbb{Z}\}, \quad (5)$$

where the dot products of the vectors \mathbf{u}_1 and \mathbf{u}_2 with the vectors \mathbf{r}_1 and \mathbf{r}_2 satisfy $\langle \mathbf{u}_l, \mathbf{r}_m \rangle = 2\pi \delta_{l,m}$ with the Kronecker delta $\delta_{l,m}$ for all $l, m \in \{1, 2\}$ [6]. The bandpass-filtered object function and, thus, the ultrasound image can be recovered from the superposition if the vectors \mathbf{u}_1 and \mathbf{u}_2 prevent the copies from overlapping. The vectors \mathbf{r}_1 and \mathbf{r}_2 , given suitable vectors $\mathbf{u}_1 = (u_{1,x}, u_{1,z})^T$ and $\mathbf{u}_2 = (u_{2,x}, u_{2,z})^T$, then equal

$$\mathbf{r}_1 = \frac{2\pi}{D} \begin{pmatrix} u_{2,z} \\ -u_{2,x} \end{pmatrix} \quad \text{and} \quad \mathbf{r}_2 = \frac{2\pi}{D} \begin{pmatrix} -u_{1,z} \\ u_{1,x} \end{pmatrix} \quad (6)$$

with $D = u_{1,x}u_{2,z} - u_{1,z}u_{2,x}$. Two spatial sampling grids (4) that enable the exact recovery of the ultrasound image will now be derived.

1) *Optimal Orthogonal Grid*: The spectral grid vectors \mathbf{u}_1 and \mathbf{u}_2 prevent the copies of the bandpass-filtered object spectrum in Fig. 3 from overlapping if $\mathbf{u}_1 = (\hat{k}_{x,\text{ub}} - \hat{k}_{x,\text{lb}})\mathbf{e}_x$ and $\mathbf{u}_2 = (\hat{k}_{z,\text{ub}} - \hat{k}_{z,\text{lb}})\mathbf{e}_z$, where $\hat{k}_{x,\text{lb}}$, $\hat{k}_{x,\text{ub}}$, $\hat{k}_{z,\text{lb}}$, $\hat{k}_{z,\text{ub}}$ are the bounds (3) and $\mathbf{e}_x = (1, 0)^T$ and $\mathbf{e}_z = (0, 1)^T$ are orthonormal unit vectors. This choice results in an *orthogonal* sampling grid (4), and the spatial grid vectors (6) become $\mathbf{r}_1 = \Delta x \mathbf{e}_x$ and $\mathbf{r}_2 = \Delta z \mathbf{e}_z$ with the optimal lengths

$$\Delta x = \frac{2\pi}{\hat{k}_{x,\text{ub}} - \hat{k}_{x,\text{lb}}} \quad \text{and} \quad \Delta z = \frac{2\pi}{\hat{k}_{z,\text{ub}} - \hat{k}_{z,\text{lb}}}. \quad (7)$$

2) *Proposed Rhombic Grid*: The spectral grid vectors $\mathbf{u}_1 = \Delta u(\sqrt{3}/2, 1/2)^T$ and $\mathbf{u}_2 = \Delta u \mathbf{e}_z$ also prevent the copies of the bandpass-filtered object spectrum in Fig. 3 from overlapping if $\Delta u = \hat{k}_{z,\text{ub}} - \hat{k}_{z,\text{lb}}$, where $\hat{k}_{z,\text{lb}}$ and $\hat{k}_{z,\text{ub}}$ are the bounds (3) and $\mathbf{e}_z = (0, 1)^T$. This choice results in a 120° rhombic grid (4), which is shown in Fig. 1, and the spatial grid vectors (6) become

$$\mathbf{r}_1 = \Delta r \mathbf{e}_x \quad \text{and} \quad \mathbf{r}_2 = \Delta r \begin{pmatrix} -1/2 \\ \sqrt{3}/2 \end{pmatrix} \quad (8)$$

with the length $\Delta r = 4\pi/(\sqrt{3}\Delta u)$.

III. METHODS

The advantages of the proposed rhombic grid (8) over two orthogonal grids, which served as benchmarks, were confirmed in an experiment with a commercial multi-tissue phantom¹ (model: 040; average speed of sound: $c = 1538.75$ m/s). A SonixTouch Research system² with a linear array (model: L14-5/38; number of elements: $N_{\text{el}} = 128$, pitch: $p = 304.8 \mu\text{m}$) acquired and stored the RF signals induced by three PWs (steering angles: $\vartheta_0 = -20^\circ$, $\vartheta_1 = 0^\circ$, $\vartheta_2 = 10^\circ$) for offline processing. The excitation voltage was a single cycle at 4 MHz.

¹Computerized Imaging Reference Systems (CIRS), Inc., Norfolk, VA, USA

²Analogic Corporation, Sonix Design Center, Richmond, BC, Canada

A. Image Formation

The DAS algorithm was executed in the Fourier domain [9], [10] and used the frequencies between $f_{\text{lb}} = 2.25$ MHz and $f_{\text{ub}} = 6.75$ MHz. The field of view (FOV) was an axis-aligned square with an edge length of 39 mm and laterally centered in front of the linear array with an axial shift of 5 mm. The apodization weights derived from a Tukey window with a cosine fraction of 20 %. The wavenumber bounds in the recoverable passbands (1) were $k_{\text{lb}} = 2\pi f_{\text{lb}}/c \approx 9187.4$ rad/m and $k_{\text{ub}} = 2\pi f_{\text{ub}}/c \approx 27562.3$ rad/m. The F -number of $F = 1$ limited the angular aperture and induced the lower and upper bounds on the receive angle $\varphi_{\text{ub}} = -\varphi_{\text{lb}} \approx 26.6^\circ$. The bounds on the angular spatial frequencies in the image spectrum (3) were $\hat{k}_{x,\text{lb}} \approx -21753.1$ rad/m, $\hat{k}_{x,\text{ub}} \approx 17112.4$ rad/m, $\hat{k}_{z,\text{lb}} \approx 16850.9$ rad/m, and $\hat{k}_{z,\text{ub}} \approx 55124.7$ rad/m.

B. Sampling Grids

The proposed rhombic grid used the length $\Delta u \approx 38273.8$ rad/m in the Fourier domain. The number of image voxels induced by the resulting grid vectors (8), which had the length $\Delta r \approx 189.6 \mu\text{m}$, amounted to 48703. The first orthogonal grid oversampled the image. The number of image voxels and their spacings amounted to $512 \times 512 = 262144$ and $\Delta x = \Delta z = p/4 = 76.2 \mu\text{m}$, respectively. The second orthogonal grid used the optimal spacings (7), which amounted to $\Delta x \approx 161.7 \mu\text{m}$ and $\Delta z \approx 164.2 \mu\text{m}$. The number of image voxels was $241 \times 237 = 57117$.

C. Image Post-Processing

All images, after the coherent compounding, were interpolated to the first orthogonal grid. This interpolation simplified comparisons by the mean structural similarity (SSIM) indices [11] and the relative root mean-squared errors (RMSEs). The author maintains a public version of the Matlab³ source code [12] to support the reproduction of the presented results and facilitate further research.

IV. RESULTS

The image spectra in Figs. 4(a), 4(c), and 4(e) strongly resembled the theoretical predictions. The spectrum of the oversampled image in Fig. 4(a) equaled the example in Fig. 2(b) except for artifacts. These artifacts showed outside the total recoverable passband (2) and stemmed from the FOV, whose boundedness limited the resolution of the spectral analysis and caused spectral leakage. The image spectra in Figs. 4(c) and 4(e) showed the periodic superposition that was predicted in Fig. 3. The absence of overlaps in these spectra enabled the recovery of the spectrum in Fig. 4(a) and, thus, the corresponding image in Fig. 4(b). The images in Figs. 4(d) and 4(f), for this reason, were visually identical to the image in Fig. 4(b).

Mean SSIM indices above 96.6 % and relative RMSEs below 6.8 % confirmed the visual equivalence of all images in Figs. 4(b), 4(d), and 4(f), as summarized in Table I. The

³The MathWorks, Inc., Natick, MA, USA

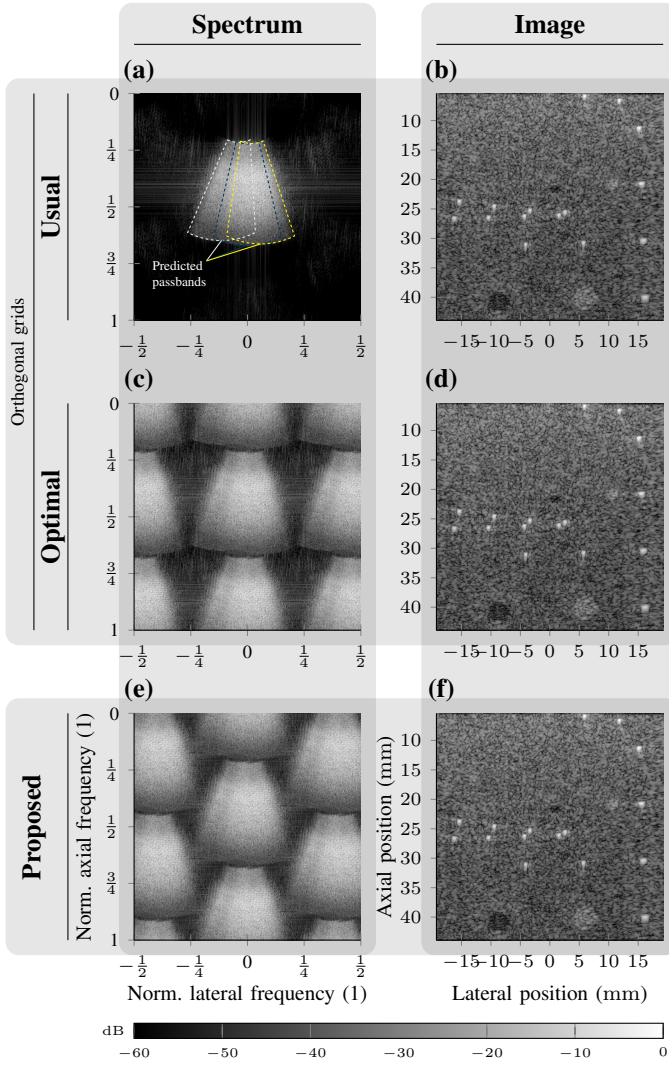


Fig. 4. Results for the multi-tissue phantom. The images show the spectra (left column) and the absolute voxel values (right column) for three steered PWs and (a), (b) the usual orthogonal grid, (c), (d) the optimal orthogonal grid with the spacings (7), and (e), (f) the proposed rhombic grid with the vectors (8). Both images in (d) and (f) were interpolated to the usual orthogonal grid in (b) to simplify comparisons. The axes in both columns are identical. The angular spatial frequencies were normalized by $8\pi/p$.

TABLE I. Mean structural similarity (SSIM) indices and relative root mean-squared errors (RMSEs) achieved by the optimal orthogonal grid and the proposed rhombic grid.

Grid type	Voxel number	Mean SSIM (%)	Rel. RMSE (%)
Usual orthogonal	262 144	100.0	0.0
Optimal orthogonal	57 117	96.9	6.4
Proposed	48 703	96.6	6.8

optimal orthogonal grid achieved slightly better mean SSIM indices and relative RMSEs than the proposed rhombic grid. This difference was probably caused by numerical interpolation errors. The proposed rhombic grid, however, reduced the number of image voxels by 81.4 % and 14.7 % in comparison to the usual and optimal orthogonal grids, respectively. Less

image voxels usually imply lower computational costs and lower memory consumption if the costs of the interpolation are negligible.

V. CONCLUSION

The proposed rhombic grid (8), as shown in Table I, maintained the image quality but reduced the number of image voxels by up to 81.4 %. This reduction translated into reductions in both the computational costs and the memory consumption. The costs of the additional interpolation (see Sect. III-C) become irrelevant if the number of steering angles per compound image is large enough. Details of the theory, such as (i) a rigorous derivation of the recoverable passbands (1) and (2) based on wave acoustics and (ii) the effects of the bounded FOV, were left to an additional publication. Future research will optimize the usage of nonorthogonal regular grids and adapt the theory to incident diverging waves and volumetric ultrasound imaging (UI). Diverging waves are superpositions of steered PWs so that the theory is applicable with only a few modifications. The author speculates that the body-centered cubic grid can outperform orthogonal grids in the three-dimensional space. The required extension of the theory is simple.

REFERENCES

- [1] G. Montaldo, M. Tanter, J. Bercoff, N. Benech, and M. Fink, "Coherent plane-wave compounding for very high frame rate ultrasonography and transient elastography," *IEEE Trans. Ultrason., Ferroelectr., Freq. Control*, vol. 56, no. 3, pp. 489–506, Mar. 2009.
- [2] M. Tanter and M. Fink, "Ultrafast imaging in biomedical ultrasound," *IEEE Trans. Ultrason., Ferroelectr., Freq. Control*, vol. 61, no. 1, pp. 102–119, Jan. 2014.
- [3] V. Perrot, M. Polichetti, F. Varray, and D. Garcia, "So you think you can DAS? A viewpoint on delay-and-sum beamforming," *Ultrasonics*, vol. 111, p. 106309, Mar. 2021.
- [4] M. F. Schiffner, "Random incident waves for fast compressed pulse-echo ultrasound imaging," *arXiv:1801.00205v2*, Mar. 2019. [Online]. Available: <https://arxiv.org/abs/1801.00205>
- [5] B. Berthon, P. Morichau-Beauchant, J. Porée, A. Garofalakis, B. Tavittian, M. Tanter, and J. Provost, "Spatiotemporal matrix image formation for programmable ultrasound scanners," *Phys. Med. Biol.*, vol. 63, no. 3, p. 03NT03, Feb. 2018.
- [6] D. P. Petersen and D. Middleton, "Sampling and reconstruction of wave-number-limited functions in N -dimensional euclidean spaces," *Inform. Control*, vol. 5, no. 4, pp. 279–323, Dec. 1962.
- [7] A. J. Devaney, *Mathematical Foundations of Imaging, Tomography and Wavefield Inversion*, 1st ed. Cambridge: Cambridge University Press, Jul. 2012.
- [8] M. F. Schiffner and G. Schmitz, "Plane wave pulse-echo ultrasound diffraction tomography with a fixed linear transducer array," in *Acoust. Imaging*, ser. Acoust. Imaging, A. Nowicki, J. Litniewski, and T. Ku-jawska, Eds. Springer Netherlands, 2012, vol. 31, pp. 19–30.
- [9] —, "Frequency-dependent F-number increases the contrast and the spatial resolution in fast pulse-echo ultrasound imaging," in *2021 IEEE Int. Ultrasonics Symp. (IUS)*, Xi'an, China, Sep. 2021, pp. 1–4.
- [10] —, "A low-rate parallel Fourier domain beamforming method for ultrafast pulse-echo imaging," in *2016 IEEE Int. Ultrasonics Symp. (IUS)*, Tours, Sep. 2016, pp. 1–4.
- [11] Z. Wang and A. C. Bovik, "Mean squared error: Love it or leave it? A new look at Signal Fidelity Measures," *IEEE Signal Process. Mag.*, vol. 26, no. 1, pp. 98–117, Jan. 2009.
- [12] M. F. Schiffner, "Rhombic grids for coherent plane-wave compounding," https://github.com/mschiffn/rhombic_grids, 2022.